A coupled optical-electrical-thermal model of the bifacial photovoltaic module

Wenbo Gu, Tao Ma*, Meng Li, Lu Shen, Yijie Zhang

School of Mechanical Engineering, Shanghai Jiao Tong University, Shanghai, China

HIGHLIGHTS

- A novel coupled optical-electrical-thermal model of the bifacial PV module is developed.
- Global irradiances of the front and rear sides are calculated by view factor and irradiance model.
- Over 22% of the average bifacial gain can be achieved via yearly performance estimation.
- Suggestions for optimizing the bifacial PV module performance are proposed.

GRAPHICAL ABSTRACT
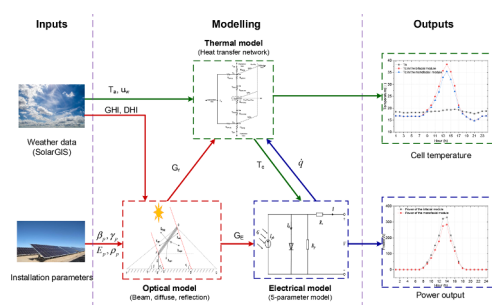
ARTICLE INFO

ABSTRACT

The bifacial photovoltaic (PV) technology has become prevalent in the global market in recent years as it can simultaneously collect the sunlight from both front and rear sides to achieve high power generation, however, there is limited attention from academic circle on this new technology particularly theory study in multiphysics simulation. This paper develops a comprehensive optical-electrical-thermal model for the bifacial PV module, in which the global irradiances of the tilted front and rear surfaces are obtained through the optical model, the cell temperature through the thermal model, and the power output through the electrical model accordingly. After validation, the coupled model is employed to conduct daily and yearly performance estimations, demonstrating 25.58% and 28.21% of the daily bifacial gain for sunny and cloudy days, respectively, and more than 22% of the yearly bifacial gain for Hong Kong and Shanghai. Besides, it is found that the bifacial gain under low irradiance is relatively high due to high diffuse fraction, indicating that bifacial modules have an advantage in adapting to various weather conditions, especially cloudy days. Furthermore, some suggestions are proposed to optimize the bifacial module by considering the effects of various installation and weather parameters on the PV generation. A tracking bifacial module, installed at an optimum tilt angle with high albedo, elevation, irradiance and wind velocity, but low ambient temperature, could achieve high energy yield, while a bifacial module facing east with high albedo, tilt angle, elevation, diffuse fraction, ambient temperature and wind velocity could achieve high bifacial gain.

1. Introduction

At present, more than 840 million people in the world still have no access to electricity though electrification level reaches a new stage [1]. Even worse, most people with no electricity live in uneconomic and even underpopulated areas, thus, it is still a huge challenge to supply

---

* Corresponding author.
  E-mail address: tao.ma@connect.polyu.hk (T. Ma).

these people with electricity. Unlike the conventional energies, the renewable energies, especially solar photovoltaic (PV) power, are ideal and suitable for the electricity supply to such areas because of the abundance and cost-effective characteristics. Moreover, an army of cities have been forced to transform conventional fuel structure to nonfossil and low-carbon energy resources including PV power because of the global dramatic energy demand and increasing environmental concerns globally [2,3]. Therefore, the PV industry is ushered in a stage of rapid development, increasing sharply from 15 GW in 2008 to 505 GW in 2018 for global PV cumulative capacity [4]. However, high levelized cost of energy (LCOE) and heavily dependence on government subsides make PV power generation hard to compete with the traditional energies in some situations.

In recent years, the bifacial PV (bPV) technology has exerted an increasingly peculiar fascination on renewable energy market because of its high electricity production by absorbing the sunlight from both sides of the PV panel compared with the mono-facial PV (mPV). This trend has become more and more obvious since the new PV policy implemented by Chinese government in 2018 [5,6]. Besides lower LCOE, the bPV modules have longer lifetime for the glass-glass structure compared with the traditional glass-backsheet module configurations, because double glass modules have lower cell temperature [7,8], and rear glass can still stand unfavorable environment. However, ordinary backsheet is gradually pulverized after being exposed to ultra-violet rays on the ground and suffers from gradual failure due to gaps and intrusion of water vapor [9,10]. In real applications, bPV modules are widely-used in various scenarios, such as noise barriers [11] and the facade of a building [12]. Those benefits will promote the development of bPV modules among all kinds of PV technologies, expanding its market share from less than 5% in 2016 to 30% in 2027 [13].

Dating back to 1980s for the history of bPV technology, Cuevas et al. [14] demonstrated that bPV cells had a huge potential in producing more electricity compared to mPV ones, up to 50%. Whereas such a high benefit value is not always accessible in real-world environment. All kinds of negative effects can influence the performance of bPV modules, including fluctuation of irradiance, temperature, shading [15], soiling [16], manufacturing process [17], etc. Unlike the convectional mPV modules with abundant theory and experimental data, the lack of reliable power predictions for the bPV modules gradually becomes a vast barrier to impulse a number of investors to chase relevant economic profits [18].

To break through these jungles, some research groups devoted themselves to improving bPV modules from new manufacturing process continuously, including quantum dots [19] and up converters [20]. Besides, a lot of efforts have been made to study the performance of bPV modules under current production technology from multiple perspectives. Wei et al. [21] claimed that the bPV modules could produce more electricity compared with mPV ones, up to 15% on sand and 30% on snow through some experiments. Yu et al. [22] replaced the traditional backsheet with a transparent one to encapsulate a bPV module and compared their monthly energy benefits with regular modules, 3–4% addition yield could be achieved. Abotaleb et al. [23] installed two bPV modules under two different installation conditions in the desert environment. It was found that an inclined module at 22° facing south produced 14% higher energy than that at 90° facing east because of higher solar radiation on the surface of the module. An experimental study conducted by Araki et al. [24] concluded that the electricity produced by rear side is contributed to one third of all electricity for a bPV system facing southwest.

Besides experimental investigations on bifacial gain, more attentions are captured on numerical simulations. Yusufoglu et al. [25] developed a model for simulating PV power output with revision of ground reflection and found that the bPV module had a potential of producing more energy with higher elevation and albedo coefficient. Wang et al. [26] deduced that bPV modules performed better in the case of high latitude, reflection coefficient and clearance distance away

from the front row. Sun et al. [13] demonstrated the performance of bPV modules from a global perspective, indicating that global bifacial gain boosted from 10% to 30% when the reflection coefficient rose from 0.25 to 0.5. A novel method was proposed by Singh et al. [27] to determine the irradiances of front and rear sides by measuring the short current, which were proportional to irradiance. Rodríguez-Gallegos et al. [28] used the value of LCOE to determine which is more cost-effective PV technology for the bPV and mPV. The results show that bPV modules for latitudes above 40° are more cost-effective in spite of albedo. However, for latitude below 40°, bPV modules would be less cost-effective unless the albedo was higher than a minimum value, 0.12–0.30. LCOE is also evaluated in Ref. [29], indicating that LCOE could be reduced by 2–6% after replacing mPV modules with bPV ones.

As indicated above, the bPV technology has become prevalent in the global PV market in recent years, while limited attention was received from academic circle on this new technology, particularly theory studies in multiphysics modelling. It is widely acknowledged that the bPV power generation not just includes optical and electrical processes, but also the typical thermodynamic process, and these three physical domains are tightly coupled. Therefore, a comprehensive multi-physics simulation model for the bPV module is rather necessary. Besides, the whole bPV power was always expressed as a linear addition of the front side power output under standard test conditions (STC) and particular rear-side irradiance listed in a table from manufacturers. However, the power of bPV modules does not vary linearly with the irradiance, such simple superposition of front- and rear-side powers will lead to great deviation when estimating bPV performance and comparing it with the mPV. Therefore, the nonlinear behavior of PV modules with irradiance should be taken into account. Moreover, the irradiance fluctuates greatly and depends on various factors, including installation location and weather parameters, which were rarely qualified and discussed in literature. For example, beam, diffuse and reflected irradiance from ground are always associated with ground albedo, tilt angle and so on, thus, it is necessary to understand how they affect each other and how to calculate their performance accurately. In this context, a coupled optical-electrical-thermal (O-E-T) model is developed in this study. During modelling process, front and rear irradiances are calculated accordingly on the basis of irradiance and view factor model. The electrical model is developed according to the specifications provided by manufacturers and referring to the standard of IEC 60904-1-2 published in 2019 [30]. Particularly, unsteady state, all various layers, and various climate conditions are considered in thermal model to make them more practical to real-world environment.

The remaining parts of the paper is organized as follows. Section 2 gives a detailed description of a bPV and mPV module. The coupled models, including optical, electrical and thermal models are illustrated and presented in Section 3. The simulation process including coupling and solving of the model is exhibited in Section 4. Results are shown in Section 5, in which the coupled model after validation is employed to discuss daily and yearly estimations, and the effects of installation and weather parameters on the performance of bPV modules. Finally, some conclusions of the whole study are listed in Section 6.

2. Bifacial PV module vs mono-facial PV module

In order to compare the performance of a bPV module, a frameless glass-glass mPV module is taken as a reference. Fig. 1 presents the structure configurations of the bPV and mPV modules. There are totally five layers in the these two modules, including front glass, upper ethylene-vinyl acetate copolymer (EVA), PV cells, lower EVA and rear glass, of which the areas are assumed as the same, while there are some differences between bPV and mPV cells, including back anti-reflection coating and back contacts.

A market available bPV module [31] and mPV module [32] are employed in this study for comparison. The key specifications of the PV modules provided by manufacturers are listed in Table 1, where MPP
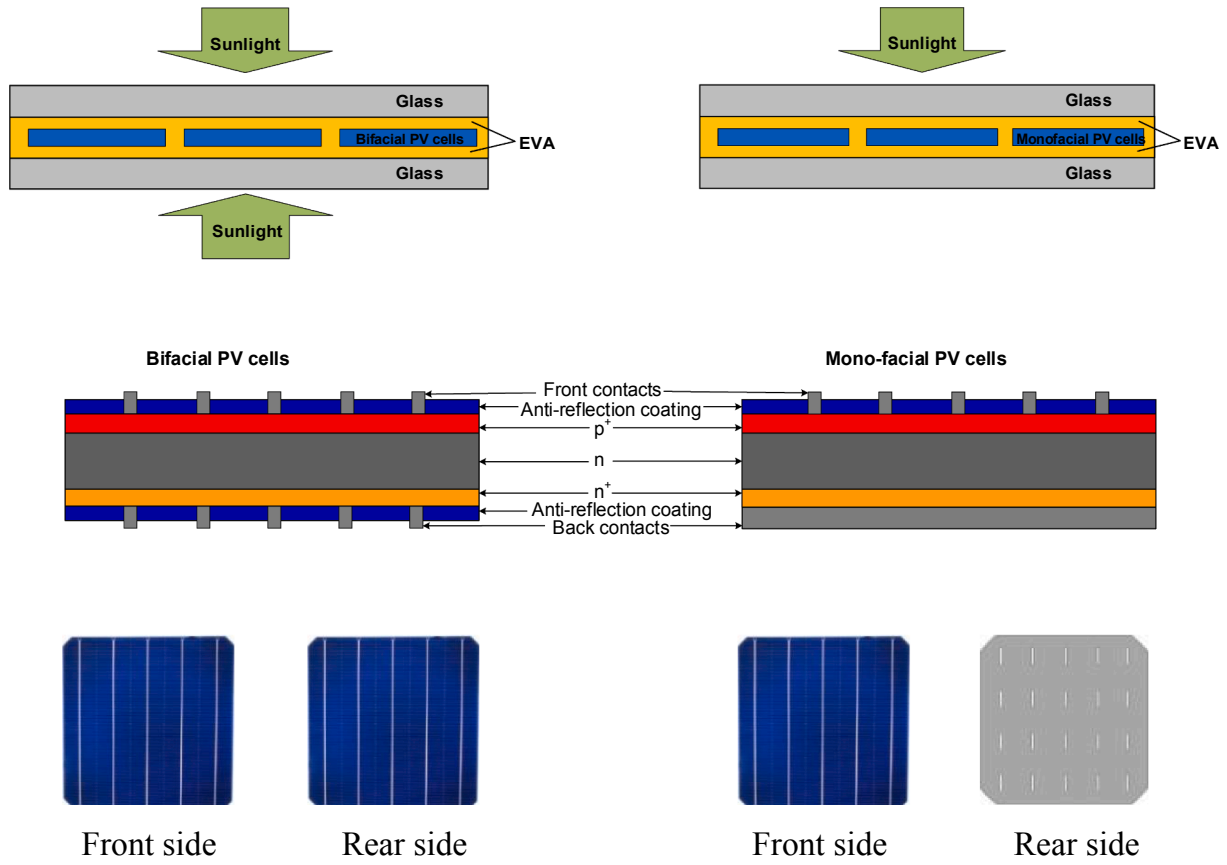
Fig. 1. Structure configurations and appearance: (a) bPV module; (b) mPV module.

refers to maximum power point.

Some physical properties, such as specific heat, and thermal conductivity, of glass, EVA and solar cells are listed in Table 2, which are necessary for the thermal model.

3. Optical-electrical-thermal modelling

A coupled O-E-T model is developed in this section to reveal the relationship among sunlight, electricity and heat. In the O-E-T model, some proper approximations are made as below for simplification:

(1) The numerical simulation is developed under 1D and unsteady-state heat transfer process, meaning that the heat flux and temperature values are just various along the thickness direction and time.
(2) The thermal losses via radiation and convection just involves the front and rear surface of the PV module, neglecting thermal losses

from the edge of the module to environment.
(3) Physical parameters of the materials in the whole system are taken as constant and independent of temperature.
(4) The structures of the bPV and mPV modules are both symmetrical, meaning that the physical properties of front and rear glasses, upper

Table 2
Physical properties of each layer [33–35].

Physical properties	Parameter	Glass	EVA	Silicon cells
Specific heat (J/(kg·K))	C_p	790	1675	700
Thickness (mm)	δ	2.5	0.5	0.4
Density (kg/m³)	ρ	2500	1070	2330
Thermal conductivity (W/(m·K))	λ	1.8	0.35	148
Emissivity	ε	0.85	/	/
Absorptivity	α	0.018	/	/
Transitivity	τ	0.95	/	/

Table 1
Key parameters of PV modules.

Specification	bPV module		mPV module
Testing condition	Front side	Rear side	/
Open-Circuit Voltage at STC ($V_{oc,ref}$)	44.5 V	44.1 V	47.4 V
Short-Circuit Current at STC ($I_{sc,ref}$)	9.96 A	8.53 A	9.64 A
Voltage at MPP at STC ($V_{mp,ref}$)	37.9 V	37.7 V	38.93 V
Current at MPP at STC ($I_{mp,ref}$)	9.38 A	8.00 A	9.12 A
Maximum Power at STC ($P_{max,ref}$)	355 W	302 W	355 W
Number of cells in a module	72 (6 × 12)		72 (6 × 12)
Dimension of a solar cell	156.75 mm × 156.75 mm		156.75 mm × 156.75 mm
Temperature coefficient of $I_{sc,ref}$ (α)	0.048%/°C		0.044%/°C
Temperature coefficient of $V_{oc,ref}$ (β)	−0.30%/°C		−0.30%/°C
Temperature coefficient of $P_{max,ref}$ (γ)	−0.38%/°C		−0.41%/°C

and lower EVA are identical.

(5) The distance of PV array is long enough to neglect the effect of reflection and shading from adjacent row on the irradiance distribution of the PV panel.

(6) The energy yield from the mPV module is assumed to be the same as the front side of the bPV.

3.1. Optical model

The optical model is first developed to understand sunlight travel path and then calculate front and rear irradiances, which are the basic parameters for estimating power generation.

3.1.1. Irradiance model

For the irradiance model of a tilted panel, weather data especially global horizontal irradiance (GHI) and diffuse horizontal irradiance (DHI) are required as the basic inputs of the model, which can be obtained from the database such as SolarGIS. Then the front- and rear-side global irradiances can be calculated accordingly.

(a) The front-side global irradiance G_F [36–38]:

$$G_F = G_b{}^F + G_d{}^F + G_r{}^F = (GHI - DHI) \cdot R_b{}^F + DHI \cdot X_{F,sky} + GHI \cdot \rho_p \cdot X_{F,grd} \tag{1}$$

where the superscript 'F' refers to front side, G_b is the beam irradiance, G_d is the diffuse irradiance, G_r is the reflection irradiance, GHI is global horizontal irradiance, DHI is diffuse horizontal irradiance, $X_{F,sky}$ is the view factor of front panel to sky, $X_{F,grd}$ is the view factor of front panel to ground, ρ_p is the albedo of the ground, and $R_b{}^F$ is the ratio of front tilted irradiance and horizontal irradiance, which can be obtained as:

$$R_b{}^F = \begin{cases} \dfrac{\cos \theta^F}{\cos \theta_Z{}^F}, & \gamma_p - \pi/2 \leqslant w \leqslant \gamma_p + \pi/2 \\ 0, & w < \gamma_p - \pi/2 \text{ or } w > \gamma_p + \pi/2 \end{cases} \tag{2}$$

where γ_p is the azimuth of PV panel, and θ, θ_Z and w is the incident angle, zenith angle, and hour angle, respectively, which can be calculated according to Ref. [39].

(b) Similarly, the rear-side global irradiance G_R can be obtained as [36–38]:

$$G_R = G_b{}^R + G_d{}^R + G_r{}^R = (GHI - DHI) \cdot R_b{}^R + DHI \cdot X_{R,sky} + GHI \cdot \rho_p \cdot X_{R,usgrd} + DHI \cdot \rho_p \cdot X_{R,sgrd} \tag{3}$$

where the superscript 'R' refers to rear side, $X_{R,sky}$ is the view factor of rear panel to sky, $X_{R,usgrd}$ is the view factor of rear panel to unshaded ground, $X_{R,sgrd}$ is the view factor of rear panel to shaded ground and $R_b{}^R$ is the ratio of rear tilted irradiance and horizontal irradiance, just replacing tilt angle with minus tilt angle in the equation of $R_b{}^F$, which can be expressed as:

$$R_b{}^R = \begin{cases} 0, & \gamma_p - \pi/2 \leqslant w \leqslant \gamma_p + \pi/2 \\ \dfrac{\cos \theta^R}{\cos \theta_Z{}^R}, & w < \gamma_p - \pi/2 \text{ or } w > \gamma_p + \pi/2 \end{cases} \tag{4}$$

3.1.2. View factor model

It can be clearly seen from Eqs. (1)–(4) that the view factor is an essential parameter during the process of irradiance calculation. To demonstrate the view factors vividly, various view factors of a PV module with a height of H_p, elevation of E_p, and tilt angle of β_p are presented in Fig. 2. It can be obviously observed that there are two view factors for front panel, $X_{F,sky}$, and $X_{F,grd}$, while there are three view factors for rear panel, namely $X_{R,sky}$, $X_{R,sgrd}$, and $X_{R,unsgrd}$.

(a) View factor of front side to sky X_{F-sky}:

$$X_{F-sky} = \frac{X_{OF-sky}{}^F \cdot \overline{OF} - X_{AF-sky}{}^F \cdot \overline{AF}}{\overline{OA}} \tag{5}$$

where $X_{OF-sky}{}^F$ and $X_{AF-sky}{}^F$ is the view factor of assumed OF and AF front panel to the sky, respectively, which can be expressed by [40]:

$$X_{OF-sky}{}^F = X_{AF-sky}{}^F = \frac{1 + \cos \beta_p}{2} \tag{6}$$

where β_p is inclined angle of the PV panel.

X_{F-sky} can be obtained as Eq. (7) after substituting Eq. (6) into Eq. (5):

$$X_{F-sky} = \frac{1 + \cos \beta_p}{2} \tag{7}$$

(b) View factor of front side to ground X_{F-grd}:

$$X_{F-grd} = \frac{X_{OF-grd}{}^F \cdot \overline{OF} - X_{AF-grd}{}^F \cdot \overline{AF}}{\overline{OA}} \tag{8}$$

where $X_{OF-grd}{}^F$ and $X_{AF-grd}{}^F$ is the view factor of assumed OF and AF front panel to the ground, respectively, which can be given by [40]:

$$X_{OF-grd}{}^F = X_{AF-grd}{}^F = \frac{1 - \cos \beta_p}{2} \tag{9}$$

View factor of front side to ground X_{F-grd} can be obtained as Eq. (10) after substituting Eq. (9) into Eq. (8):

$$X_{F-grd} = \frac{1 - \cos \beta_p}{2} \tag{10}$$

(c) View factor of rear side to sky X_{R-sky}:

$$X_{R-sky} = \frac{X_{OF-sky}{}^R \cdot \overline{OF} - X_{AF-sky}{}^R \cdot \overline{AF}}{\overline{OA}} \tag{11}$$

where $X_{OF-sky}{}^F$ and $X_{AF-sky}{}^F$ is the view factor of assumed OF and AF front panel to the sky, respectively, which can be represented as:

$$X_{OF-sky}{}^R = X_{AF-sky}{}^R = \frac{1 + \cos \beta_p}{2} \tag{12}$$

X_{R-sky} can be calculated as Eq. (13) after substituting Eq. (12) into Eq. (11):

$$X_{R-sky} = \frac{1 - \cos \beta_p}{2} \tag{13}$$

(d) View factor of rear side to unshaded ground $X_{R-usgrd}$:

$$X_{R-usgrd} = X_{R-DQ} + X_{R-CF} \tag{14}$$

where X_{R-DQ} and X_{R-CF} is the view factor of rear PV panel to DQ and CF panel, respectively, which can be rewritten as Eqs. (15) and (16):

$$X_{R-DQ} = \frac{X_{OF-DQ}{}^R \cdot \overline{OF} - X_{AF-DQ}{}^R \cdot \overline{AF}}{\overline{OA}} \tag{15}$$

$$X_{R-CF} = \frac{X_{OF-CF}{}^R \cdot \overline{OF} - X_{AF-CF}{}^R \cdot \overline{AF}}{\overline{OA}} \tag{16}$$

where $X_{OF-DQ}{}^R$ is the view factor of rear OF panel to DQ panel, $X_{AF-DQ}{}^R$ is the view factor of rear AF panel to DQ panel, $X_{OF-CF}{}^R$ is the view factor of rear OF panel to CF panel, $X_{AF-CF}{}^R$ is the view factor of rear AF panel to CF panel, and all of them can be calculated as Eqs. (17)–(20):

$$X_{OF-DQ}{}^R = X_{OF-FQ}{}^R - X_{OF-FD}{}^R = \frac{1 + \cos \beta_p}{2} - \frac{\overline{OF} + \overline{FD} - \overline{OD}}{2\overline{OF}} \tag{17}$$

$$X_{AF-DQ}{}^R = X_{AF-FQ}{}^R - X_{AF-FD}{}^R = \frac{1 + \cos \beta_p}{2} - \frac{\overline{AF} + \overline{FD} - \overline{AD}}{2\overline{AF}} \tag{18}$$

$$X_{OF-CF}{}^R = \frac{\overline{OF} + \overline{CF} - \overline{OC}}{2\overline{OF}} \tag{19}$$
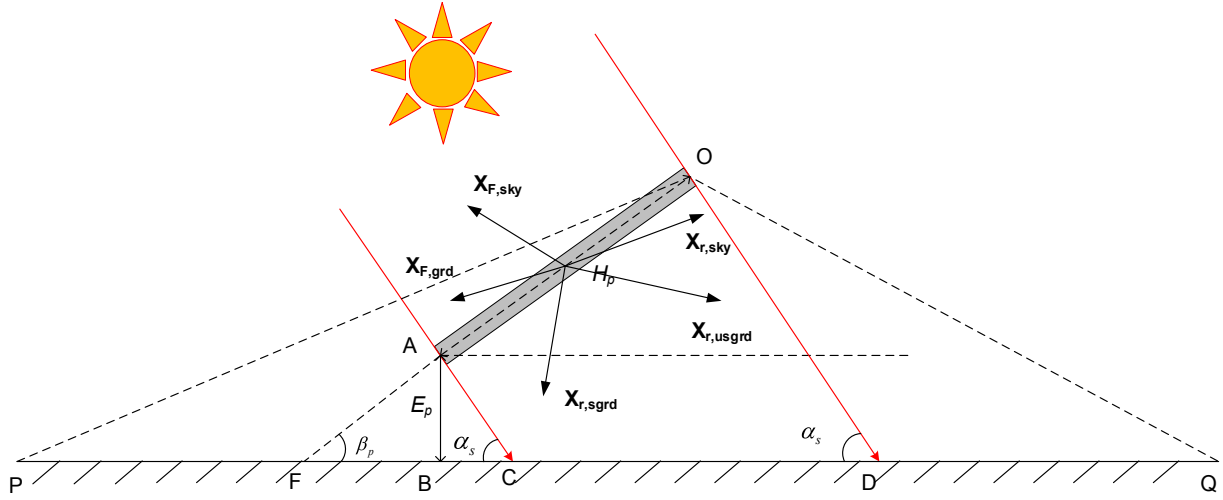
Fig. 2. Schematic of a PV module's view factor.

$$X_{AF-CF}{}^R = \frac{\overline{AF} + \overline{CF} - \overline{AC}}{2\overline{AF}} \quad (20)$$

where $\quad \overline{OA} = H_p; \quad \overline{OF} = \sqrt{(H_p \cos\beta_p + \frac{E_p}{\tan\beta_p})^2 + (E_p + H_p \sin\beta_p)^2};$

$\overline{AF} = \frac{E_p}{\sin\beta_p}; \quad \overline{OD} = \sqrt{(H_p \cos\beta_p - \frac{E_p \cos\alpha_s + H_p \sin(\alpha_s + \beta_p)}{\sin\alpha_s})^2 + (E_p + H_p \sin\beta_p)^2};$

$\overline{AC} = \frac{E_p}{\sin\alpha_s}; \overline{CF} = E_p(\frac{1}{\tan\alpha_s} + \frac{1}{\tan\beta_p}); \overline{FD} = \frac{H_p}{\sin\alpha_s} \sin(\alpha_s + \beta_p) + \frac{H_p}{\tan\beta_p} + \frac{H_p}{\tan\alpha_s};$

$\overline{OC} = \sqrt{(H_p \cos\beta_p - \frac{E_p}{\tan\alpha_s})^2 + (E_p + H_p \sin\beta_p)^2};$

$\overline{AD} = \sqrt{(\frac{E_p \cos\alpha_s + H_p \sin(\alpha_s + \beta_p)}{\sin\alpha_s})^2 + E_p{}^2}.$

(e) View factor of rear side to shaded ground X_{R-sgrd} [40]:

$$X_{R-sgrd} = \frac{\overline{OC} + \overline{AD} - (\overline{AC} + \overline{OD})}{2\overline{OA}} \quad (21)$$

3.2. Electrical model

3.2.1. Mathematic model expression

To calculate PV power output, a well-known equivalent circuit using 5 parameters is employed compromising simplification and accuracy [41,42]. The equivalent circuit is presented in Fig. 3, and related mathematical model for a PV cell based on the Shockley diode equation can be presented as Eq. (22) [43,44]. The model presented in this section has been developed and validated in authors' previous study [45,46].

$$I = I_{ph} - I_d - I_p = I_{ph} - I_0 \left[\exp\left(\frac{V + I \cdot R_s}{V_t}\right) - 1 \right] - \frac{V + R_s I}{R_p} \quad (22)$$

where I_{ph} is the photo current, I_d is the diode current, I_p is the current through the parallel resistance, I_0 is the diode reserve saturation
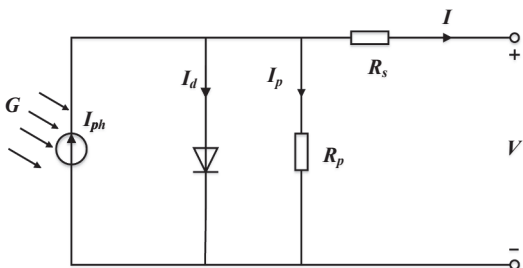

Fig. 3. Equivalent circuit for a solar cell.

current, R_s is the series resistance, R_p is the parallel resistance, $V_t = n \cdot K \cdot T / q$ is the diode thermal voltage, n is the diode ideality factor, q is electronic charge (1.602E−19C), K is the Boltzmann's constant (1.381E−23J/K) and T is the cell temperature.

As for a PV module with many solar cells, Eq. (22) can be rewritten as Eq. (23) [44]:

$$I = I_{ph} - I_0 \left[\exp\left(\frac{1}{V_t}(\frac{V}{N_s} + I \cdot R_s)\right) - 1 \right] - \frac{1}{R_p}\left(\frac{V}{N_s} + R_s I\right) \quad (23)$$

where N_s is the number of solar cells connected in series for each module.

It is obviously seen that there are five unknown parameters to be determined, including I_{ph}, I_0, R_s, R_p and V_t, which are actually inaccessible from manufacturers. Therefore, the parameters extraction under STC needs to be done at first and it is then pushed from STC to non-STC.

3.2.2. Parameters extraction

As known, the 5-parameter extraction under STC is the foundation. The five unknown parameters can be rewritten as: $I_{ph,ref}$, $I_{0,ref}$, $R_{s,ref}$, $R_{p,ref}$ and $V_{t,ref}$. Then the Eq. (23) can be rewritten as Eq. (24):

$$I = I_{ph,ref} - I_{0,ref}\left[\exp\left(\frac{V + I \cdot R_{s,ref}}{N_s V_{t,ref}}\right) - 1 \right] - \frac{V + R_{s,ref} I}{R_{p,ref}} \quad (24)$$

where $I_{ph,ref}$, $I_{0,ref}$, $R_{s,ref}$, $R_{p,ref}$, and $V_{t,ref}$ are the related parameters under STC.

(1) Thermal voltage under STC $V_{t,ref}$

Thermal voltage under STC $V_{t,ref}$ can be represented as Eq. (25) according to the definition of the voltage temperature coefficient β at open-voltage point [42]:

$$V_{t,ref} = \frac{\beta T_{ref} - V_{oc,ref}}{\frac{N_s T_{ref}\alpha}{I_{ph,ref}} - 3N_s - \frac{E_g N_s}{K T_{ref}}} \quad (25)$$

where α is the temperature coefficient of the short circuit, E_g is the band gap (1.7936e−19 J).

(2) Photo current at STC $I_{ph,ref}$

The photo current at STC $I_{ph,ref}$ can be obtained as Eq. (26) based on the condition ($V = 0$, $I = I_{sc,ref}$) [47]:

$$I_{ph,ref} \approx I_{sc,ref} \quad (26)$$

(3) Diode reserve saturation current at STC $I_{0,ref}$

The diode reserve saturation current at STC $I_{0,ref}$ can be expressed as Eq. (27) after the condition ($V = V_{oc,ref}$, $I = 0$) is substituted into Eq. (24) [47]:

$$I_{0,ref} = I_{sc,ref} \exp\left(\frac{-V_{oc,ref}}{N_s V_{t,ref}}\right) \tag{27}$$

(4) Parallel resistance at STC $R_{p,ref}$

Parallel resistance at STC $R_{p,ref}$ can be given as Eq. (28) according to the property of MPP, zero derivative of power to voltage [42]:

$$R_{p,ref} = \frac{(V_{mp,ref} - I_{mp,ref} R_{s,ref})(V_{mp,ref} - N_s V_{t,ref})}{(V_{mp,ref} - I_{mp,ref} R_{s,ref})(I_{sc,ref} - I_{mp,ref}) - N_s V_{t,ref} I_{mp,ref}} \tag{28}$$

(5) Series resistance at STC $R_{s,ref}$

Eq. (24) can be rewritten as Eq. (29) after substituting Eq. (28) and the condition of MPP ($I = I_{mp,ref}$ and $V = V_{mp,ref}$) into Eq. (24) [42]:

$$I_{mp,ref} = I_{ph,ref} - I_{0,ref}\left[\exp\left(\frac{V_{mp,ref} + I_{mp,ref} R_{s,ref}}{N_s V_{t,ref}}\right) - 1\right]$$
$$- \frac{(V_{mp,ref} + I_{mp,ref} R_{s,ref})[(V_{mp,ref} - I_{mp,ref} R_{s,ref})(I_{sc,ref} - I_{mp,ref}) - N_s V_{t,ref} I_{mp,ref}]}{(V_{mp,ref} - I_{mp,ref} R_{s,ref})(V_{mp,ref} - N_s V_{t,ref})} \tag{29}$$

It is obvious to see that only one unknown variable of series resistance $R_{s,ref}$ needs to be calculated in Eq. (29) through the 'fzero' solver in Matlab.

(6) 5-parameter extraction under non-STC

Then, the related characteristic parameters under non-STC can be calculated by means of the cell temperature and equivalent irradiance and represented as Eqs. (30)–(36) [43,44,48]:

$$I_{ph} = \frac{G_E}{G_{ref}}(I_{ph,ref} + \alpha \cdot (T - T_{ref})) \tag{30}$$

$$I_0 = I_{0,ref}\left(\frac{T}{T_{ref}}\right)^3 \exp\left[\frac{qE_g}{K}\left(\frac{1}{T_{ref}} - \frac{1}{T}\right)\right] \tag{31}$$

$$R_s = R_{s,ref} \tag{32}$$

$$R_p = \frac{G_{ref}}{G_E} R_{p,ref} \tag{33}$$

$$V_t = \frac{T}{T_{ref}} V_{t,ref} \tag{34}$$

$$G_E = G_F + G_R \cdot \varphi \tag{35}$$

$$\varphi = \begin{cases} \min\left(\frac{I_{sc,ref,R}}{I_{sc,ref,F}}, \frac{P_{\max,ref,R}}{P_{\max,ref,F}}\right), & \text{Bifacial module,} \\ 0, & \text{Monofacial module.} \end{cases} \tag{36}$$

where G_E is the equivalent irradiance, φ is the bifacial coefficient [30].

3.2.3. Electricity yield and bifacial gain

The purpose of parameters extraction is to calculate actual power output of the module. Based on STC characteristic curve and related parameters in Fig. 4, new characteristic curve and parameters under non-STC can be obtained in red color according to the demonstration of Sections 3.2.1 and 3.2.2.

Therefore, actual power output can be calculated as Eq. (37):

$$P_{PV} = (1 - SL) \cdot I_{mp} \cdot V_{mp} \tag{37}$$

where P_{PV} is the PV electrical generation, SL is soiling loss [49], I_{mp} and
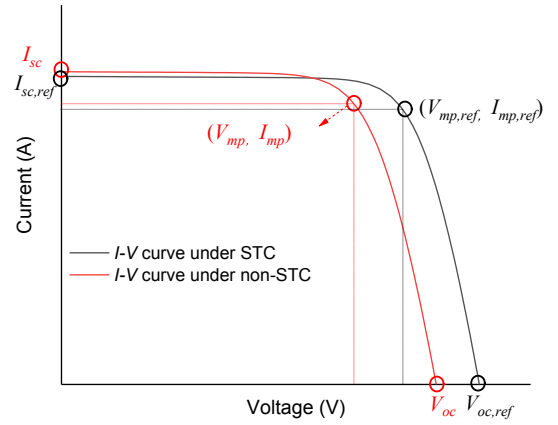

Fig. 4. The characteristic curves and parameters.

V_{mp} is the current and voltage at MPP under non-STC, respectively.

To assess the advantage of a bPV module compared to a mPV one, bifacial gain, relative increase of the electricity production, is defined as Eq. (38) [13,14]:

$$\text{Bifacial gain } (\%) = (Y_{Bi} - Y_{Mono}) / Y_{Mono} \times 100 \tag{38}$$

where Y_{Bi} and Y_{Mono} are electricity yields of bPV and mPV modules in kWh.

3.3. Thermal model

The actual power output can be calculated when the equivalent irradiance and the cell temperature are known. The irradiance can be calculated by optical model or measured by the pyranometer. However, the cell temperature cannot be measured by thermocouple directly. Therefore, modelling of the thermal behavior of bPV modules is essential to simulate the cell temperature accurately.

3.3.1. Equivalent thermal circuit

To develop the thermal model, it is necessary to acquire the energy flows, which can be represented as Fig. 5 by means of the equivalent thermal circuit. It is easy to observe that the input energy is the total received irradiance. For the front panel, a part of sunlight is reflected by glass, and a small portion is absorbed by glass, while the rest is transmitted through the glass and absorbed by PV cells. The absorption of rear panel is similar to the front side. It is worth noting that the input energy just comes from front irradiance for mPV modules, while the source of power generation for bPV modules is the irradiances of both sides. In spite of the type of the modules, the photon passes its energy to the carrier so that irradiance energy is transformed into electricity due to PV effect. The extra and unabsorbable energy is transformed into heat, which is then conducted to the front and rear glasses, and finally dissipated by convection and radiation.

3.3.2. Thermal resistance definitions

As described in Section 3.3.1, thermal resistance is a key parameter, which can be divided into three categories according to heat transfer method, namely radiative, convective, and conductive thermal resistances.

For radiative thermal resistance, the energy via radiation dissipates between the surfaces and environment. Hence, radiative resistance of front and rear glasses, $R_{rad,g}$ and $R_{rad,rg}$ can be given by:

$$R_{rad,g} = \frac{1}{h_{rad,g} A} \tag{39}$$

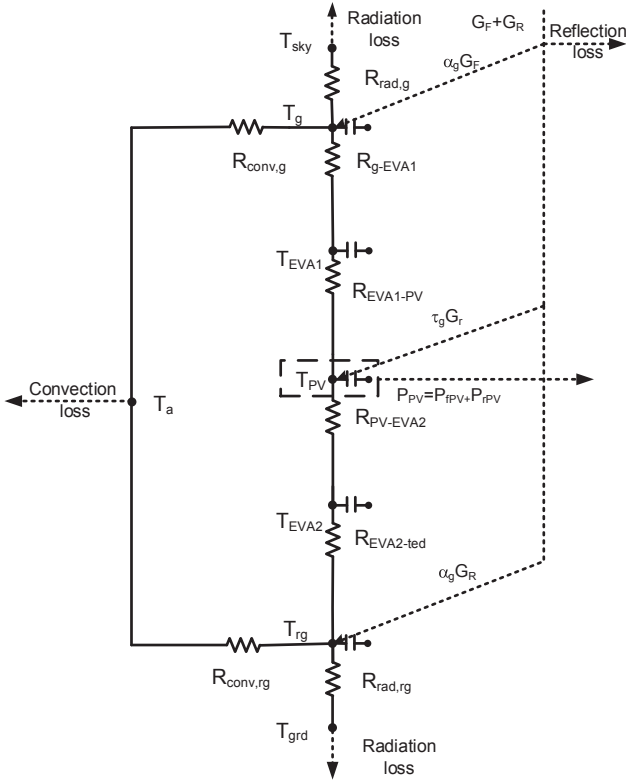$$R_{rad,rg} = \frac{1}{h_{rad,rg} A} \tag{40}$$

Fig. 5. Equivalent thermal circuit for the PV modules.

where $h_{rad,g}$ and $h_{rad,rg}$ are radiative heat coefficients of front and rear glasses, which can be obtained by:

$$h_{rad,g} = \varepsilon_g \sigma (T_{sky}^2 + T_g^2)(T_{sky} + T_g) \tag{41}$$

$$h_{rad,rg} = \varepsilon_g \sigma (T_{grd}^2 + T_{rg}^2)(T_{grd} + T_{rg}) \tag{42}$$

where ε_g is the glass emissivity, σ is the Stefan–Boltzmann constant, 5.67e-8 W/(m^2·K^4), T_g and T_{rg} are the front and rear glasses temperature, T_{grd} is the ground temperature, which is assumed to be equal to the ambient temperature in this study, and T_{sky} is the sky temperature, which can be expressed as [50]:

$$T_{sky} = 0.0552 T_a^{1.5} \tag{43}$$

where T_a is ambient temperature.

Similar to radiation, heat transfer via convection also involves front and rear glasses and surrounding environment. Thus the convective thermal resistance can be obtained as Eq. (44):

$$R_{conv,g} = R_{conv,rg} = \frac{1}{h_{conv,g} A} \tag{44}$$

where $R_{conv,g}$ and $R_{conv,rg}$ are convective thermal resistances of front and rear glasses, and $h_{conv,g}$ and $h_{conv,rg}$ are the convective heat coefficients of front and rear glasses, which can be represented respectively as [51,52]:

$$h_{conv,g} = h_{conv,rg} = 2.8 + 3.0u \tag{45}$$

where u is wind velocity.

Conversely, conduction just occurs between two adjacent layers inside PV module, which all can be calculated as:

$$R_{i-j} = \frac{\delta_i}{2\lambda_i A_i} + \frac{\delta_j}{2\lambda_j A_j} \tag{46}$$

where the subscript '*i*' and '*j*' refer to the layer i, j, involving front glass, upper EVA, PV cells, lower EVA, and rear glass, R_{i-j} is the conductive thermal resistance between the layer i and j, δ is the thickness, λ is the

thermal conductivity, and A is the area.

3.3.3. Heat transfer equations

Based on the energy transfer network and thermal resistance definitions described in Sections 3.3.1 and 3.3.2, the related heat transfer equations can be listed as Eqs. (47)–(52):

(a) For the front glass:

$$C_{p,g} \delta_g A \rho_g \frac{dT_g}{dt} = \alpha_g G_F A + \frac{T_{EVA1} - T_g}{R_{EVA1-g}} - \frac{T_g - T_a}{R_{conv,g}} - \frac{T_g - T_{sky}}{R_{rad,g}} \tag{47}$$

where $C_{p,g}$ is the glass specific heat, δ_g is the glass thickness, ρ_g is the glass density, α_g is the absorptivity of glass, t is the time, G_F is irradiance of front side, A is the area value of the PV module, T_g is the front glass temperature, T_{EVA1} is the upper EVA temperature, T_a is the ambient temperature, T_{sky} is the sky temperature, R_{EVA1-g} is the conductive thermal resistance between upper EVA and front glass, and $R_{conv,g}$ and $R_{rad,g}$ are the convective and radiative thermal resistances of front glass.

(b) For the upper EVA:

$$C_{p,EVA} \delta_{EVA} A \rho_{EVA} \frac{dT_{EVA1}}{dt} = \frac{T_{PV} - T_{EVA1}}{R_{PV-EVA1}} - \frac{T_{EVA1} - T_g}{R_{EVA1-g}} \tag{48}$$

where $C_{p,EVA}$ is the EVA specific heat, δ_{EVA} is the EVA thickness, ρ_{EVA} is the EVA density, T_{PV} is the PV cell temperature, and $R_{PV-EVA1}$ is the conductive thermal resistance between PV and upper EVA.

(c) For the PV cells:

$$C_{p,PV} \delta_{PV} A \rho_{PV} \frac{dT_{PV}}{dt} = (\tau_g G_r A - P_{PV}) - \frac{T_{PV} - T_{EVA1}}{R_{PV-EVA1}} - \frac{T_{PV} - T_{EVA2}}{R_{PV-EVA2}} \tag{49}$$

where $C_{p,PV}$ is the PV cell specific heat, δ_{PV} is the PV layer thickness, ρ_{PV} is the PV layer density, τ_g is the glass transitivity, T_{EVA2} is the lower EVA temperature, $R_{PV-EVA2}$ is the conductive thermal resistance between PV layer and lower EVA, and G_r is the received irradiance, which can be obtained by Eq. (50):

$$G_r = \begin{cases} G_F + G_R, & \text{Bifacial module,} \\ G_F, & \text{Monofacial module.} \end{cases} \tag{50}$$

where G_R is irradiance of rear side.

(d) For the lower EVA:

$$C_{p,EVA} \delta_{EVA} A \rho_{EVA} \frac{dT_{EVA2}}{dt} = \frac{T_{PV} - T_{EVA2}}{R_{PV-EVA2}} - \frac{T_{EVA2} - T_{rg}}{R_{EVA2-rg}} \tag{51}$$

where T_{EVA2} is the lower EVA temperature, T_{rg} is rear glass temperature, and $R_{EVA2-rg}$ is the conductive thermal resistance between lower EVA and rear glass.

(e) For the rear glass:

$$C_{p,g} \delta_g A \rho_g \frac{dT_{rg}}{dt} = \alpha_g G_R A + \frac{T_{EVA2} - T_{rg}}{R_{EVA2-rg}} - \frac{T_{rg} - T_a}{R_{conv,rg}} - \frac{T_{rg} - T_{grd}}{R_{rad,rg}} \tag{52}$$

where $R_{conv,rg}$ and $R_{rad,rg}$ are the convective and radiative thermal resistances of rear glass.

4. Coupling and decoupling

4.1. Optical-electrical-thermal models coupling

In this section, the optimal model, electrical model and thermal model are coupled. As presented in Fig. 6, the inputs of the optical model includes weather parameters (GHI and DHI) and installation parameters (tilt angle β_p, azimuth angle γ_p, elevation E_p and albedo ρ_p).
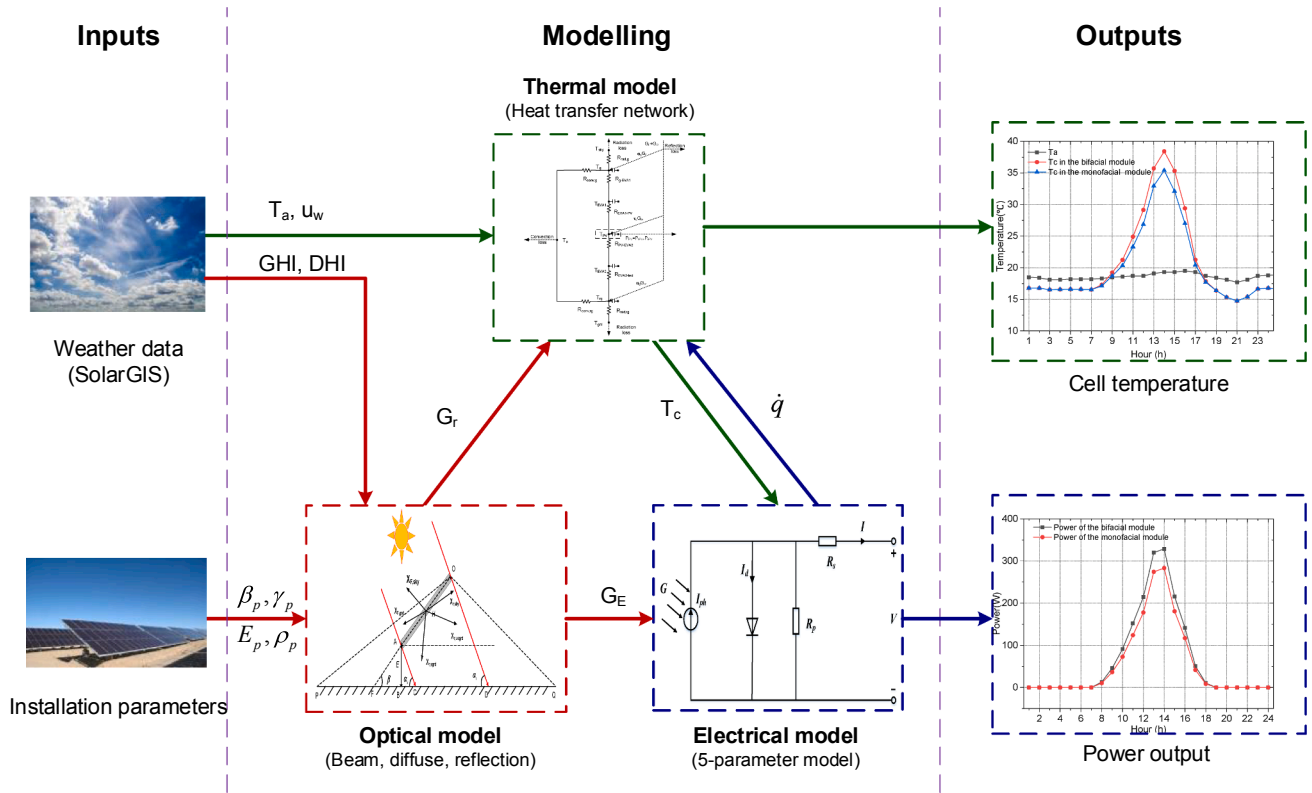
Inputs

Modelling

Outputs

Fig. 6. Schematic diagram of the coupling models.

After calculating beam, diffuse and reflection radiation, the optical model outputs the equivalent irradiance G_E and received irradiance G_r. The equivalent irradiance together with the output of thermal model (cell temperature T_c) acts as the inputs of the electrical model, and through this method the power generation are calculated. Then the rest of the absorbed solar energy is transformed into heat as an internal heat source $\dot{q}$, together with received irradiance, wind velocity and ambient temperature acting as the inputs for the thermal model. It should be highlighted that there is a closed loop between electrical and thermal model, indicating that the values of the cell temperature and internal heat source can be calculated accordingly by means of equation iteration.

4.2. Decoupling and solving process

Based on the schematic diagram of the coupled model in Fig. 6, the related model has been programed in MATLAB R2017b. To demonstrate the decoupling and solving process clearly, a flowchart is drawn in Fig. 7, which can be divided into three steps:

(1) Meteorological data and PV specifications are input into the O-E-T model. The electrical equivalent irradiance can be calculated on the basis of the optical model with weather data. PV characteristic parameters under STC can be obtained with PV specifications as stated earlier.
(2) The stage is to attain temperature distribution by continuous iteration. The temperature distribution, especially the cell temperature is a crucial parameter linking electrical and thermal model. On one hand, the cell temperature is intrinsically dependent on the theory of energy conservation, developed in thermal model. On the other hand, a high cell temperature has negative impact on PV power output, about $-0.4\%/K$ for silicon solar cell. The specific iterative procedure can be illustrated as below. The power output from PV and the value of the internal heat source can be calculated in the electrical model after initializing the temperature

distribution. Next the new temperature distribution can be computed in the thermal model, and then new values of temperature will replace old ones to continue the numerical iteration, until the maximum relative error is less than $1e-5$ and the iteration number is higher than 8760.
(3) Solving process comes to the last stage, post processing, where the temperature distribution and PV electricity production are calculated accordingly.

5. Results and discussion

Based on the models developed in Section 3 and coupling/solving processes presented in Section 4, the temperature distribution and power output for a bPV module can be obtained. In this section, the feasibility of the mathematical model is discussed through validation, then the daily and yearly performance estimations are made to exhibit the bPV performance. Finally, parametric analyses including installation and weather parameters are done to reveal how these parameters affect the performance of bPV technology.

5.1. Validation of the model

As indicated above, the coupled model consists of three sub models: optical model, electrical model and thermal model. Optical model is referred to Liu and Jordan model [39] and some related knowledge of view factor; electrical model [42] and thermal model [53] for mPV modules have already studied in our previous study, in which these models have been validated though experimental tests or other recognized research in this field. The electrical and thermal models for bPV modules are very similar to those for mPV modules. Thus, now it is sufficient to validate the coupled model only. However, as this is a frontier research, there is rare study on O-E-T modelling and experiment of bPV module, so it is challenging to have a solid validation on the couple model. For better validation in this paper, PVsyst software and Sun model [13] are also used to calculate the energy yield of the
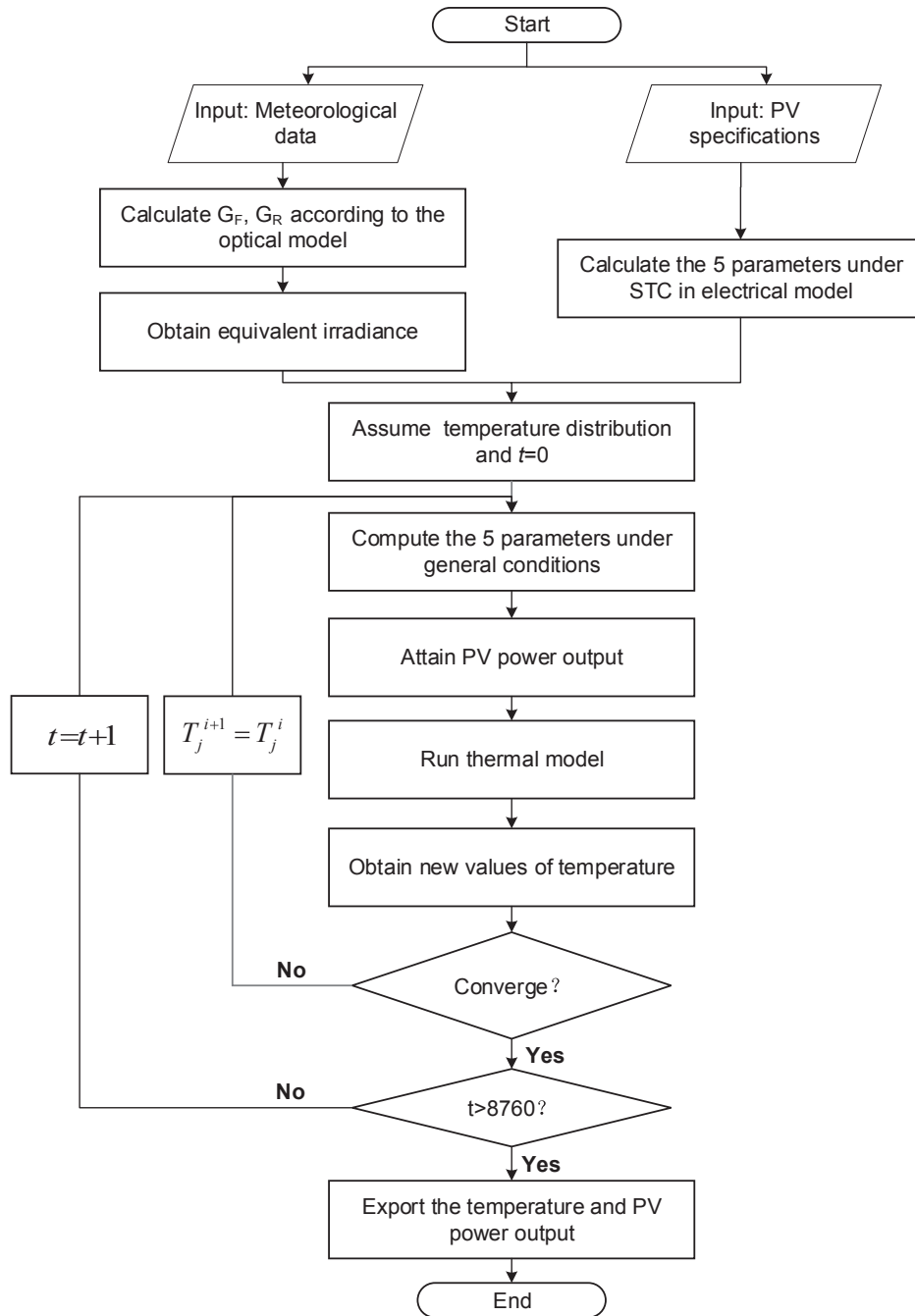
```
                              ( Start )
                    ┌─────────────┴─────────────┐
        ┌───────────────────────┐      ┌───────────────────┐
       / Input: Meteorological /      / Input: PV         /
      /  data                 /      /  specifications   /
     └───────────────────────┘      └───────────────────┘
                │                             │
   ┌────────────────────────┐    ┌────────────────────────────┐
   │ Calculate G_F, G_R     │    │ Calculate the 5 parameters │
   │ according to the       │    │ under STC in electrical    │
   │ optical model          │    │ model                      │
   └────────────────────────┘    └────────────────────────────┘
                │                             │
   ┌────────────────────────┐                │
   │ Obtain equivalent      │                │
   │ irradiance             │                │
   └────────────────────────┘                │
                └──────────────┬─────────────┘
                    ┌─────────────────────────┐
                    │ Assume temperature      │
                    │ distribution and t=0    │
                    └─────────────────────────┘
                                │
                    ┌─────────────────────────┐
                    │ Compute the 5 parameters│
                    │ under general conditions│
                    └─────────────────────────┘
                                │
                    ┌─────────────────────────┐
                    │ Attain PV power output  │
                    └─────────────────────────┘
                                │
                    ┌─────────────────────────┐
                    │ Run thermal model       │
                    └─────────────────────────┘
                                │
                    ┌─────────────────────────┐
                    │ Obtain new values of    │
                    │ temperature             │
                    └─────────────────────────┘
                                │
              No       ◇ Converge? ◇
                                │ Yes
              No       ◇ t>8760? ◇
                                │ Yes
                    ┌─────────────────────────┐
                    │ Export the temperature  │
                    │ and PV power output     │
                    └─────────────────────────┘
                                │
                            ( End )
```

Boxes on the left branch: $t=t+1$ and $T_j^{i+1} = T_j^{i}$

Fig. 7. Flow chart of decoupling and solving process.

bPV modules after importing the whole year weather data of Shanghai in 2017 into. Fig. 8 compares the monthly electricity production from the bifacial module by the proposed model, PVsyst software and Sun model. As presented in Fig. 8, the electricity calculated by the proposed model shows good agreement with the PVsyst and Sun model. It is noted that electricity yield from the proposed model is slightly higher in summer and lower in winter than that from PVsyst and Sun model, which can be explained by the accuracy of the thermal model. For simplification, a simple temperature model is employed in PVsyst and Sun model as the thermal model, namely Faiman model [54], which actually overestimates the cell temperature in summer and underestimates in winter. In the proposed model, the computation efficiency could be a little lower than PVsyst and Sun model due to its complex iteration. However, the simulated results could be more accurate, because the effect of various factors (ambient temperature, irradiance,

wind velocity, radiative loss and unsteady state) on cell temperature, and coupling relationship among sunlight, electricity and heat are taken into consideration to make it more accessible to the real-world environment.

5.2. Daily performance estimation

The performance of PV modules depends strongly on local climatic conditions. For daily performance estimation, two typical weather conditions in Shanghai, namely sunny and cloudy, are carried out to depict the benefits of bPV and mPV modules.

According to the results in Fig. 9, the bPV energy yield coincides with the irradiance, but some deviations appear round noon time the sunny day due to the temperature effect. For both bPV and mPV modules, they both produce higher energy yield in the sunny day than
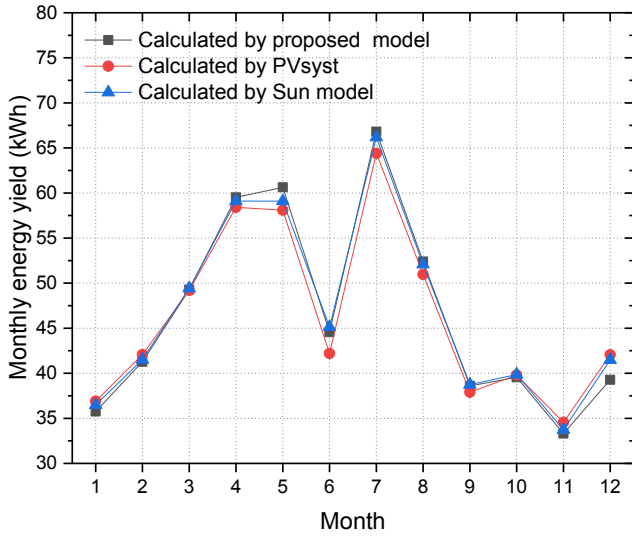
Fig. 8. The monthly energy yield calculated by different methods.

Table 3
The weather data of Shanghai and Hong Kong in 2017.

Month	GHI (kWh/m²/day)		DHI (kWh/m²/day)		T_a (°C)		u (m/s)	
	SH	HK	SH	HK	SH	HK	SH	HK
1	2.25	3.09	1.37	1.72	6.66	16.84	3.94	3.09
2	3.04	3.26	1.70	2.15	6.43	15.47	3.96	3.26
3	3.54	2.87	2.08	2.13	9.84	16.73	3.57	2.87
4	4.85	3.62	2.52	2.51	16.57	21.63	3.70	3.62
5	5.04	3.90	2.63	2.74	21.23	24.38	3.66	3.90
6	3.80	4.03	2.53	2.70	23.75	26.99	2.83	4.03
7	5.76	4.47	3.21	2.79	30.54	26.91	2.71	4.47
8	4.33	4.81	2.75	2.73	29.33	27.42	2.92	4.81
9	3.12	4.06	1.99	2.76	24.23	27.08	3.22	4.06
10	2.83	4.50	1.88	2.41	18.74	23.62	4.07	4.50
11	2.32	2.88	1.51	1.87	13.49	19.69	3.54	2.88
12	2.44	3.72	1.40	1.87	6.84	15.90	3.72	3.72
Ave.	3.61	3.77	2.09	2.32	17.30	21.89	3.49	3.77

that in the cloudy day because of the higher irradiance. However, it is interesting that the bifacial gain on the sunny day is lower than that on the cloudy day, 25.58% versus 28.21%. It can be attributed to the reason that the diffuse fraction (the ratio of diffuse irradiance and global irradiance) is high under low irradiance, resulting in that available rear irradiance is a dominator of total received irradiance for bPV modules. Therefore, the bPV technology has an advantage in adapting to various weather conditions, especially cloudy days.

5.3. Yearly performance estimation

As indicated above, the performance of bPV modules is strongly affected by weather conditions onsite. Therefore, a yearly performance estimation of bPV modules in Shanghai (SH) and Hong Kong (HK) are made to obtain some statistic results. The weather data, including GHI, DHI, ambient temperature (T_a) and wind velocity (u) of these two cities, are presented in Table 3. It can be easily observed that the irradiance, ambient temperature, and wind velocity in Hong Kong is higher and has a more uniform distribution than that of Shanghai.

Base on the developed model in Section 3, the irradiance for the bPV and mPV modules against month can be calculated and plotted in Fig. 10. It is obvious that front and rear irradiances coincide with GHI

line, and the rear-side irradiances for both Shanghai and Hong Kong share 28% of the front-side irradiance, implying that the bPV module would have produced 28% more electricity than the mPV one if temperature effect was negligible.

Electricity yield of bPV and mPV modules is plotted in Fig. 11. Over 22% of bifacial gain can be achieved in the two different climatic cities. The bPV energy yield and bifacial gain, as the representatives of bPV performance, in Hong Kong are obviously higher than those in Shanghai due to high irradiance. It is worth noting that the mPV energy yield in June for Shanghai and that in March for Hong Kong are lower than those obtained in other typical meteorological months, because there are quite a few cloudy days in those two months. However, the values of bifacial gain for the two months are still on higher stages. Again, it indicates that the bPV technology can adapt to the various weather conditions well, especially cloudy days.

In addition, bifacial gains for Shanghai and Hong Kong both reach 22% instead of 28% (irradiance increase). The difference 6% may result from temperature effect.

5.4. Parametric analyses

To optimize bPV modules, it is necessary to know how all kinds of parameters, including various installation and weather parameters, affect the performance of bPV modules. Therefore, parametric analyses of installation and weather parameters are made in this section to guide the optimization of bPV modules.
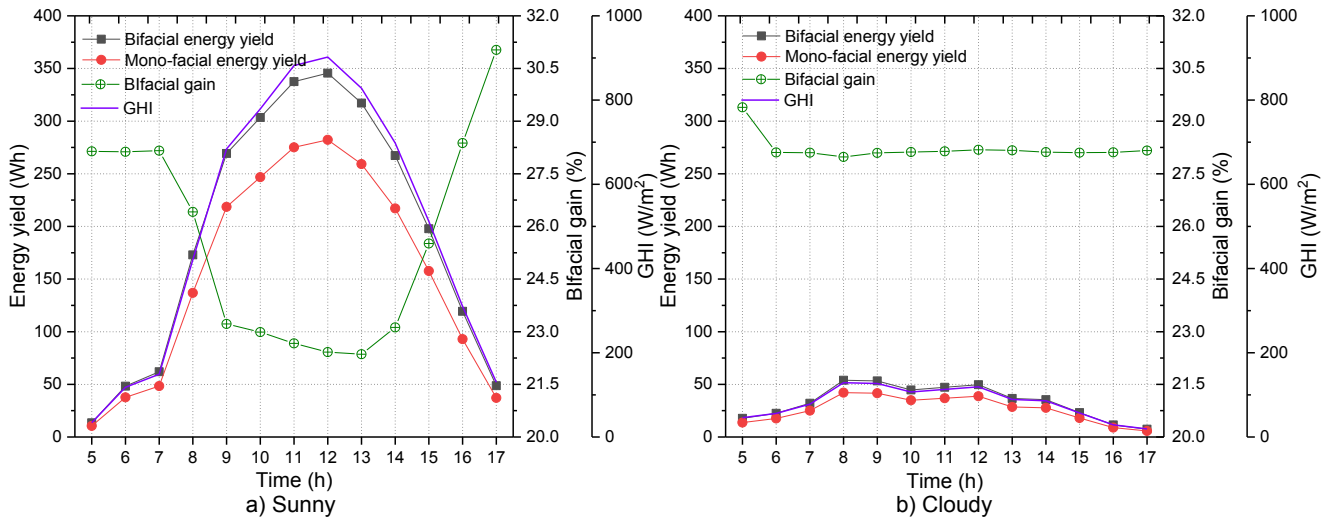

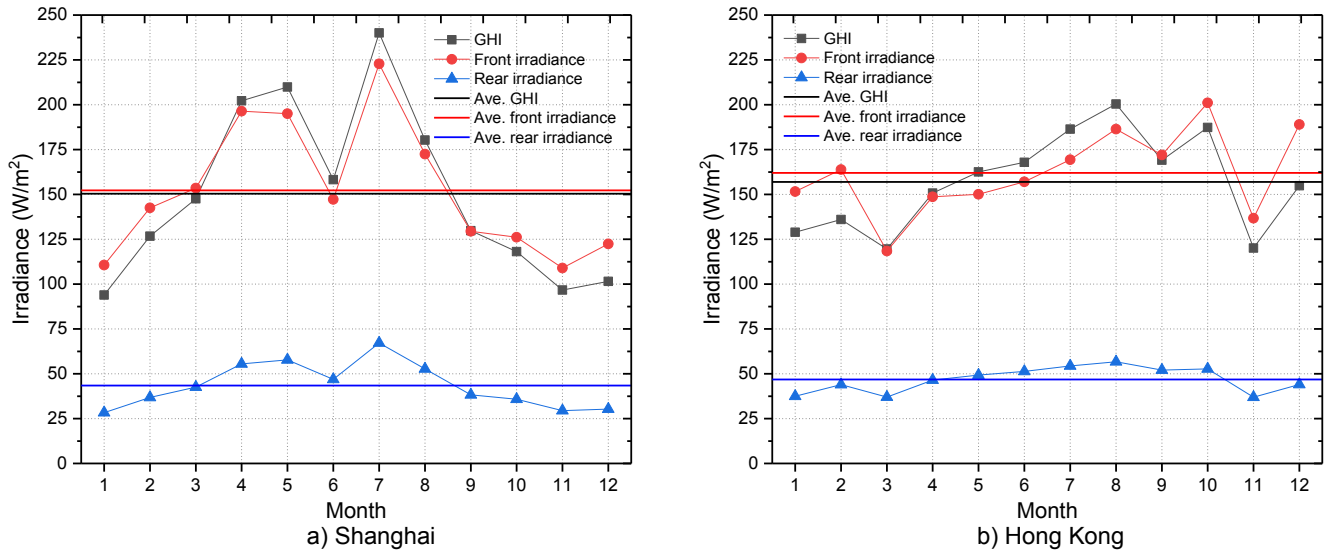**Fig. 9.** PV performance under two different cases: (a) sunny; (b) cloudy.

Fig. 10. The irradiance distribution for the bPV modules: (a) Shanghai; (b) Hong Kong.

5.4.1. Installation parameters

When it comes to installation parameters, albedo, elevation, tilt angle and azimuth angle are always involved in the simulation field of bPV modules. Hence, the annual performance of PV modules in Shanghai is simulated accordingly to assess the effects of installation parameters in this part.

5.4.1.1. Effect of albedo (ρ_p).
Effect of albedo can hardly be neglected because the reflection of ground is the main source of rear irradiance. In the light of the results in Fig. 12, albedo has a strong positive effect on the rear irradiance, resulting in that bPV energy yield grows linearly when albedo of ground rises. Therefore, the bifacial gain also faces linear growth under almost constant front irradiance, indicating that the bPV module can take advantage of its property to output more electricity in the areas of higher albedo like snowy areas and white painted field.

5.4.1.2. Effect of tilt angle (β_p).
Besides albedo, tilt angle is also

regarded as a crucial factor of PV performance. Hence, the behavior between the performance of PV modules and tilt angle is investigated in Fig. 13. It can be seen that the tilt angle increases the annual energy slightly for the bPV and mPV modules firstly and decreases rapidly until 90°, peaked at 25° and 20°. Therefore, 25° and 20° could be regarded as the optimum angles of the bPV and mPV modules onsite for maximum production, respectively. It is noted that the effect of tilt angle on the diffuse irradiance from the sky and ground is negligible, resulting in the rear energy taking up a larger share of total bPV energy yield and bifacial gain increasing with a rising tilt angle, up to 56% at 90°. The trend of bifacial gain can satisfactorily explain why bPV technology is more recommended than mPV technology in some situations, like the vertical facade of a building and vertical noise barriers.

5.4.1.3. Effect of elevation (E_p).
To reveal the relationship between PV performance and elevation, the annual energy yield and bifacial gain against elevation are plotted in Fig. 14. It can be seen that mPV energy yield seems to be insensitive to elevation, while bPV energy yield and
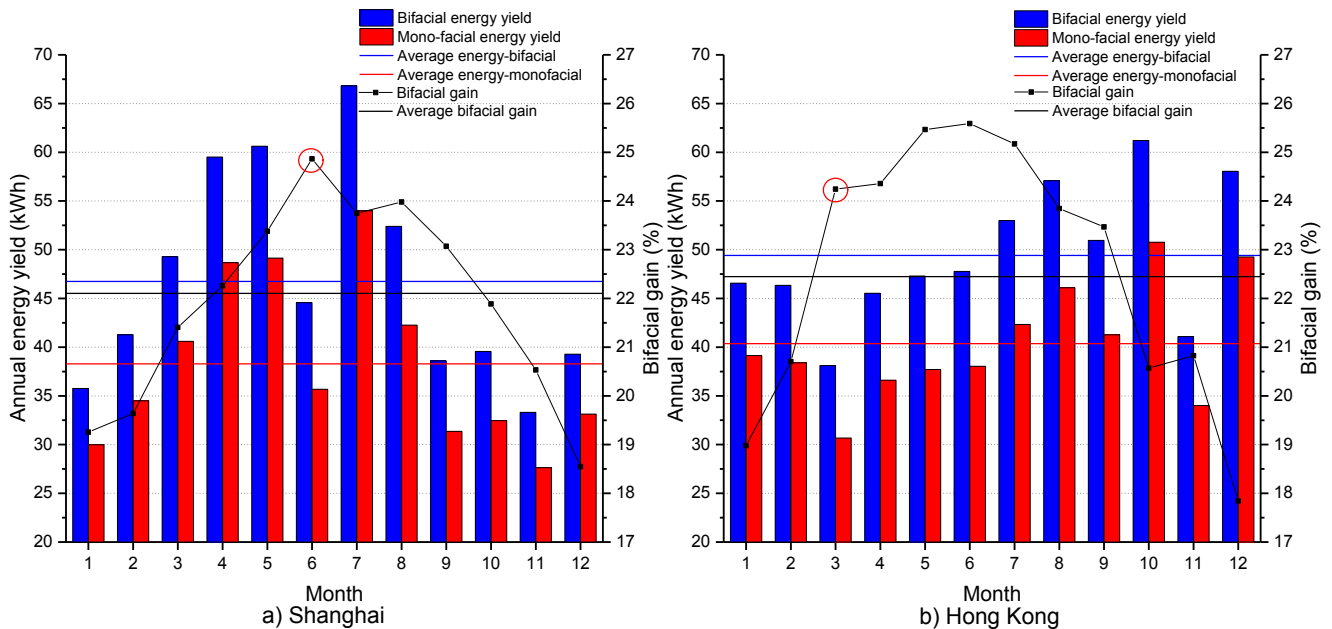

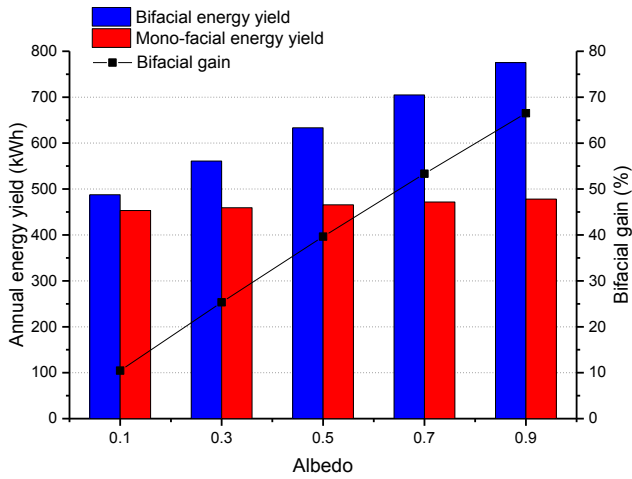**Fig. 11.** The performance of the bPV and mPV modules: (a) Shanghai; (b) Hong Kong.

Fig. 12. The effect of albedo on PV performance ($E_p = 1$ m, $\beta_p = 30°$, and $\gamma_p = 0°$).

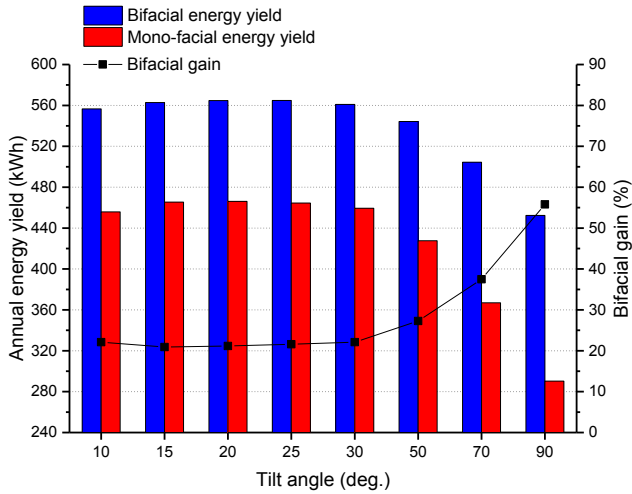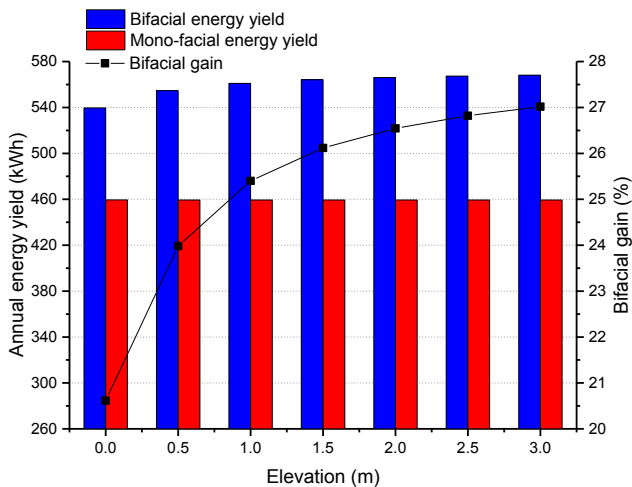**Fig. 15.** The effect of orientation on PV performance ($\rho_p = 0.3$, $\beta_p = 30°$ and $E_p = 1$).

growth rate.

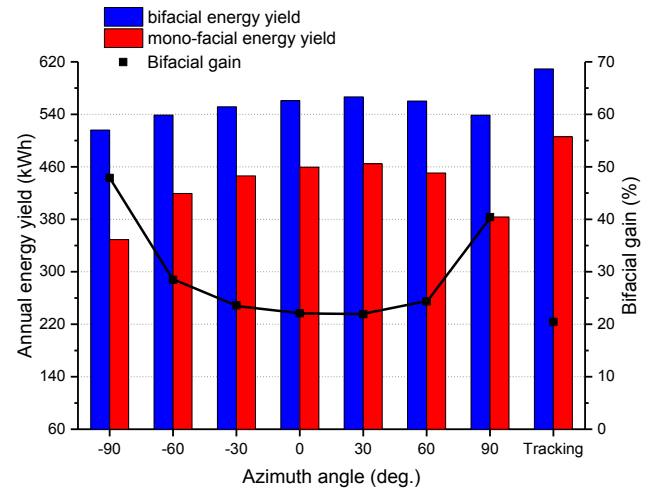Based on this study, it is recommended to raise the elevation of the bPV module to 0.5–1.5 m above ground, to achieve a good balance between electrical gain and size of space.

5.4.1.4. Effect of azimuth angle (γ_p). To evaluate the effect of orientation well, two cases, namely the fixed and tracking cases are taken into consideration. For the fixed one, seven angles at 30° interval from $-90°$ (facing east) to 90° (facing west) are considered. The performance of bPV and mPV modules is exhibited in Fig. 15.

According to the results in Fig. 15, annual energy yield varies with fixed azimuth angle, implying that orientation affects the PV performance strongly in spite of PV technology. If a tracking system is employed, the annual energy for both bPV and mPV modules are higher than fixed modules, because the modules with tracking system can receive more irradiance. However, the bifacial gain with a tracking system is lower than that of the fixed modules at any azimuth angle.

For the fixed case, mPV energy yield increases rapidly firstly, reaching the peak of energy at 30°. The bPV energy yield has the same trend as the mPV energy yield, but it varies little. Therefore, the trend of bifacial gain is quite opposite to the bPV and mPV energy yield. Low mPV energy yield with high bifacial gain indicates that adopting bPV technology is more flexible than mPV one, to break the limitation of orientation.

It is noting that PV modules produce more energy at a positive azimuth angle than those at a related negative angle, instead of the symmetry. The answer to the phenomenon is that hourly irradiance in the afternoon is higher than that in the morning from Fig. 16.

5.4.2. Weather parameters

Not only installation parameters, but also weather parameters have key effects on the performance of the PV modules. In this section, front irradiance, rear irradiance, ambient temperature and wind velocity as the weather factors are studied.

It is obviously seen from Fig. 17 that bifacial gain seems more sensitive to front and rear irradiances than ambient temperature and wind velocity. As presented in Fig. 17(a), there is nearly linear growth for bPV and mPV energy yield though bifacial gain gradually reduces when front irradiance increases. From Fig. 17(b), bPV energy yield grows continuously although mPV energy yield stays constant as rear irradiance rises, resulting in the constantly rising bifacial gain, which is similar to bPV energy yield. Therefore, a high bifacial gain of the bPV module can be achieved at high rear irradiance and low front irradiance, such conditions can take place on a cloudy day or at a high latitude where the diffuse fraction is high.
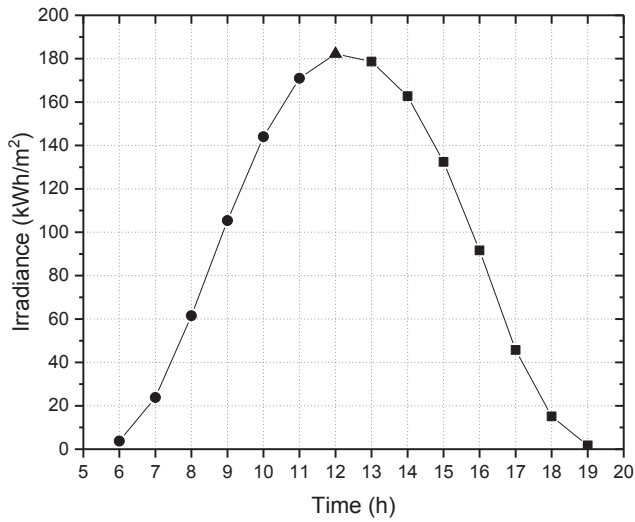

Fig. 13. The effect of tilt angle on PV performance ($\rho_p = 0.3$, $E_p = 1$ m, and $\gamma_p = 0°$).

Fig. 14. The effect of elevation on PV performance ($\rho_p = 0.3$, $\beta_p = 30°$ and $\gamma_p = 0°$).

bifacial gain accelerate at high elevation due to more reflected irradiance from the ground and less self-shading. Therefore, the bifacial gain rises by steps due to high rear irradiance, but with small

Fig. 16. Hourly irradiance of Shanghai in 2017.

As presented in Fig. 17(c) and (d), low ambient temperature and high wind velocity contribute to low cell temperature and more energy generation by strengthening the heat transfer conditions, which can explain the facts that both of bPV and mPV electrical yields are inversely proportional to ambient temperature, while proportional to wind velocity. As for the bifacial gain, it constantly increases with ambient temperature. While the bifacial gain is proportion to wind velocity, indicating that the bPV module is more sensitive to wind velocity compared with ambient temperature.

6. Conclusions

In this study, a novel coupled optical-electrical-thermal model is developed for the bifacial PV modules. After validation, the coupled model is applied to estimate electricity performance. The effects of various installation and weather parameters on the PV performance are also investigated. The main conclusions are summarized as below:

(1) Over 22% of the average bifacial gain can be achieved in both Shanghai and Hong Kong, in which rear irradiances equal to 28% of front irradiance.
(2) Bifacial modules have an advantage of adapting to various weather conditions, especially cloudy days.
(3) To achieve high bifacial energy yield, a tracking bifacial module at an optimum tilt angle with high albedo, elevation, irradiance and wind velocity, but low ambient temperature is recommended.
(4) To achieve high bifacial gain, a bifacial module facing east with high albedo, tilt angle, elevation, diffuse fraction, ambient temperature, and wind velocity is recommended.

Further in depth analyses could be performed for uneven back irradiance calculation, row spacing influence and multi-factor optimization exploration.
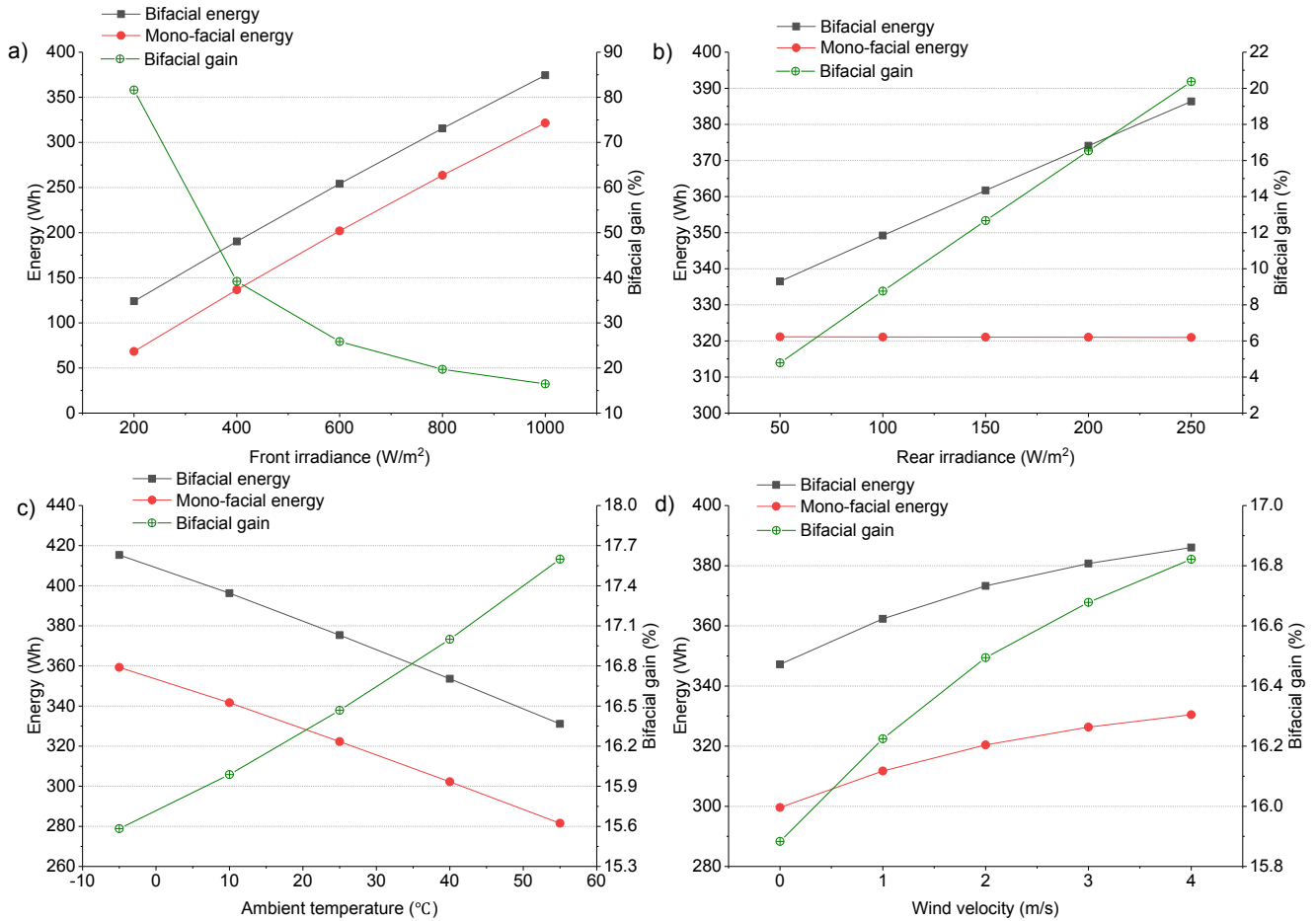

Fig. 17. The effects of weather conditions on the PV modules performance: (a) front irradiance; (b) rear irradiance; (c) ambient temperature; (d) wind velocity.

Declaration of Competing Interest

The authors declare that they have no known competing financial interests or personal relationships that could have appeared to influence the work reported in this paper.

Acknowledgements

References

[1] IEA. Tracking SDG7: The Energy Progress Report, 2019. Available: < https://www.irena.org/publications/2019/May/Tracking-SDG7-The-Energy-Progress-Report-2019 > .

[2] Chen Z, Wu L, Cheng S, Lin P, Wu Y, Lin W. Intelligent fault diagnosis of photovoltaic arrays based on optimized kernel extreme learning machine and I-V characteristics. Appl Energy 2017;204:912–31.

[3] Ma T, Østergaard PA, Lund H, Yang H, Lu L. An energy system model for Hong Kong in 2020. Energy 2014;68:301–10.

[4] REN21. Renewables 2019 Global Status Report. Available: < http://www.ren21.net/gsr-2019/pages/foreword/foreword/ > .

[5] Liang TS, Pravettoni M, Deline C, Stein JS, Kopecek R, Singh JP, et al. A review of crystalline silicon bifacial photovoltaic performance characterisation and simulation. Energy Environ Sci 2019;12:116–48.

[6] Katsaounis T, Kotsovos K, Gereige I, Basaheeh A, Abdullah M, Khayat A, et al. Performance assessment of bifacial c-Si PV modules through device simulations and outdoor measurements. Renew Energy 2019;143:1285–98.

[7] Lamers MWPE, Özkalay E, Gali RSR, Janssen GJM, Weeber AW, Romijn IG, et al. Temperature effects of bifacial modules: Hotter or cooler? Sol Energy Mater Sol Cells 2018;185:192–7.

[8] Guerrero-Lemus R, Vega R, Kim T, Kimm A, Shephard LE. Bifacial solar photovoltaics – A technology review. Renew Sustain Energy Rev 2016;60:1533–49.

[9] Carolus J, Tsanakas JA, van der Heide A, Voroshazi E, De Ceuninck W, Daenen M. Physics of potential-induced degradation in bifacial p-PERC solar cells. Sol Energy Mater Sol Cells 2019;200.

[10] Barbato M, Barbato A, Meneghini M, Tavernaro G, Rossetto M, Meneghesso G. Potential induced degradation of N-type bifacial silicon solar cells: An investigation based on electrical and optical measurements. Sol Energy Mater Sol Cells 2017;168:51–61.

[11] Faturrochman GJ, de Jong MM, Santbergen R, Folkerts W, Zeman M, Smets AHM. Maximizing annual yield of bifacial photovoltaic noise barriers. Sol Energy 2018;162:300–5.

[12] Soria B, Gerritsen E, Lefillastre P, Broquin J-E. A study of the annual performance of bifacial photovoltaic modules in the case of vertical facade integration. Energy Sci Eng 2016;4:52–68.

[13] Sun X, Khan MR, Deline C, Alam MA. Optimization and performance of bifacial solar modules: A global perspective. Appl Energy 2018;212:1601–10.

[14] Cuevas A, Luque A, Eguren J, del Alamo J. 50 Per cent more output power from an albedo-collecting flat panel using bifacial solar cells. Sol Energy 1982;29:419–20.

[15] De Groot KM, Van Aken BB. Near-field partial shading on rear side of bifacial modules. In: 7th international conference on silicon photovoltaics, Siliconpv 2017; 2017; 124: p. 532–9.

[16] Luque EG, Antonanzas-Torres F, Escobar R. Effect of soiling in bifacial PV modules and cleaning schedule optimization. Energy Convers Manage 2018;174:615–25.

[17] Shanmugam V, Chen N, Yan X, Khanna A, Nagarajan B, Rodriguez J, et al. Impact of the manufacturing process on the reverse-bias characteristics of high-efficiency n-type bifacial silicon wafer solar cells. Sol Energy Mater Sol Cells 2019;191:117–22.

[18] Nussbaumer H, Klenk M, Morf M, Keller N. Energy yield prediction of a bifacial PV system with a miniaturized test array. Sol Energy 2019;179:316–25.

[19] Pan AC, Zanesco I, Moehlecke A. Industrial bifacial silicon solar cells with up-converter and PbS quantum dots. Energy Procedia 2014;44:160–6.

[20] Pan AC, Cardoso LSG, Reis FSd. Modeling mathematical of the behavior of up converter when implemented in bifacial silicon solar cells. Energy Procedia 2016;102:80–6.

[21] Wei Q, Wu C, Liu X, Zhang S, Qian F, Lu J, et al. The glass-glass module using n-type bifacial solar cell with PERT structure and its performance. Energy Procedia 2016;92:750–4.

[22] Yu B, Song D, Sun Z, Liu K, Zhang Y, Rong D, et al. A study on electrical performance of N-type bifacial PV modules. Sol Energy 2016;137:129–33.

[23] Abotaleb A, Abdallah A. Performance of bifacial-silicon heterojunction modules under desert environment. Renew Energy 2018;127:94–101.

[24] Araki I, Tatsunokuchi M, Nakahara H, Tomita T. Bifacial PV system in Aichi Airport-site Demonstrative Research Plant for New Energy Power Generation. Sol Energy Mater Sol Cells 2009;93:911–6.

[25] Yusufoglu UA, Lee TH, Pletzer TM, Halm A, Koduvelikulathu LJ, Comparotto C, et al. Simulation of energy production by bifacial modules with revision of ground reflection. Energy Procedia 2014;55:389–95.

[26] Wang S, Wilkie O, Lam J, Steeman R, Zhang W, Khoo KS, et al. Bifacial photovoltaic systems energy yield modelling. Energy Procedia 2015;77:428–33.

[27] Singh JP, Aberle AG, Walsh TM. Electrical characterization method for bifacial photovoltaic modules. Sol Energy Mater Sol Cells 2014;127:136–42.

[28] Rodríguez-Gallegos CD, Bieri M, Gandhi O, Singh JP, Reindl T, Panda SK. Monofacial vs bifacial Si-based PV modules: Which one is more cost-effective? Sol Energy 2018;176:412–38.

[29] Patel MT, Khan MR, Sun X, Alam MA. A worldwide cost-based design and optimization of tilted bifacial solar farms. Appl Energy 2019;247:467–79.

[30] IEC. IEC TS 60904-1-2. Available: < https://webstore.iec.ch/publication/34357 > .

[31] Jolywood. JW-D72N Series high efficiency monocrystalline silicon bifacial/white glazed double glass module (model: JW-D72N Series). Available: < https://www.enf.com.cn/Product/pdf/Crystalline/5ba3385b24b61.pdf > .

[32] Astronergy. Double glass mono-facial module with transparent encapsulate material (model: CHSM6612M (DGT)). Available: < https://www.enf.com.cn/Product/pdf/Crystalline/5bebdae41916a.pdf > .

[33] Guerriero P, Codecasa L, d'Alessandro V, Daliento S. Dynamic electro-thermal modeling of solar cells and modules. Sol Energy 2019;179:326–34.

[34] Armstrong S, Hurley WG. A thermal model for photovoltaic panels under varying atmospheric conditions. Appl Therm Eng 2010;30:1488–95.

[35] Hammami M, Torretti S, Grimaccia F, Grandi G. Thermal and performance analysis of a photovoltaic module with an integrated energy storage system. Appl Sci 2017;7.

[36] Yang D. Solar radiation on inclined surfaces: Corrections and benchmarks. Sol Energy 2016;136:288–302.

[37] Sun L, Lu L, Yang H. Optimum design of shading-type building-integrated photovoltaic claddings with different surface azimuth angles. Appl Energy 2012;90:233–40.

[38] Noorian AM, Moradi I, Kamali GA. Evaluation of 12 models to estimate hourly diffuse irradiation on inclined surfaces. Renew Energy 2008;33:1406–12.

[39] Jakhrani AQ, Othman A-K, Rigit A, Samo SR, Kamboh S. Estimation of incident solar radiation on tilted surface by different empirical models. Int J Sci Res Publ 2012;2:1–6.

[40] Appelbaum J. The role of view factors in solar photovoltaic fields. Renew Sustain Energy Rev 2018;81:161–71.

[41] Ma T, Yang H, Lu L. Development of a model to simulate the performance characteristics of crystalline silicon photovoltaic modules/strings/arrays. Sol Energy 2014;100:31–41.

[42] Ma T, Gu W, Shen L, Li M. An improved and comprehensive mathematical model for solar photovoltaic modules under real operating conditions. Sol Energy 2019;184:292–304.

[43] De Soto W, Klein SA, Beckman WA. Improvement and validation of a model for photovoltaic array performance. Sol Energy 2006;80:78–88.

[44] Tian H, Mancilla-David F, Ellis K, Muljadi E, Jenkins P. A cell-to-module-to-array detailed model for photovoltaic panels. Sol Energy 2012;86:2695–706.

[45] Gu W, Ma T, Song A, Li M, Shen L. Mathematical modelling and performance evaluation of a hybrid photovoltaic-thermoelectric system. Energy Convers Manage 2019;198:111800.

[46] Ma T, Yang H, Lu L. Solar photovoltaic system modeling and performance prediction. Renew Sustain Energy Rev 2014;36:304–15.

[47] Celik AN, Acikgoz N. Modelling and experimental verification of the operating current of mono-crystalline photovoltaic modules using four- and five-parameter models. Appl Energy 2007;84:1–15.

[48] Bai J, Liu S, Hao Y, Zhang Z, Jiang M, Zhang Y. Development of a new compound method to extract the five parameters of PV modules. Energy Convers Manage 2014;79:294–303.

[49] Bhaduri S, Kottantharayil A. Mitigation of soiling by vertical mounting of bifacial modules. IEEE J Photovolt 2019;9:240–4.

[50] Soltani S, Kasaeian A, Sokhansefat T, Shafii MB. Performance investigation of a hybrid photovoltaic/thermoelectric system integrated with parabolic trough collector. Energy Convers Manage 2018;159:371–80.

[51] Watmuff JH, Charters WWS, Proctor D. Solar and wind induced external coefficients - Solar collectors. Cooperation Mediterraneenne Pour Lenergie Solaire 1977;56.

[52] Kaplani E, Kaplanis S. Thermal modelling and experimental assessment of the dependence of PV module temperature on wind velocity and direction, module orientation and inclination. Sol Energy 2014;107:443–60.

[53] Gu W, Ma T, Shen L, Li M, Zhang Y, Zhang W. Coupled electrical-thermal modelling of photovoltaic modules under dynamic conditions. Energy 2019;188.

[54] Faiman D. Assessing the outdoor operating temperature of photovoltaic modules. Prog Photovolt Res Appl 2008;16:307–15.